*R*esearch in
*A*stronomy and
*A*strophysics

^{12}CO, ^{13}CO and C^{18}O observations along the major axes of nearby bright infrared galaxies *

Qing-Hua Tan[1,2,3], Yu Gao[1], Zhi-Yu Zhang[1,2] and Xiao-Yang Xia[3]

[1] Purple Mountain Observatory, Chinese Academy of Sciences, Nanjing 210008, China;
   yugao@pmo.ac.cn
[2] Graduate School of Chinese Academy of Sciences, Beijing 100039, China
[3] Tianjin Astrophysics Center, Tianjin Normal University, Tianjin 300384, China

Abstract We present simultaneous observations of ^{12}CO, ^{13}CO and C^{18}O J=1−0 emission in 11 nearby (cz <1000 km s^{-1}) bright infrared galaxies. Both ^{12}CO and ^{13}CO are detected in the centers of all the galaxies, except for ^{13}CO in NGC 3031. We have also detected C^{18}O, CSJ=2−1 and HCO$^+$ J=1−0 emission in the nuclear regions of M82 and M51. These are the first systematical extragalactic detections of ^{12}CO and its isotopes from the PMO 14 m telescope. We have conducted half-beam-spaced mapping of M82 over an area of $4' \times 2.5'$ and major axis mapping of NGC 3627, NGC 3628, NGC 4631 and M51. The radial distributions of ^{12}CO and ^{13}CO in NGC 3627, NGC 3628 and M51 can be well fitted by an exponential profile. The ^{12}CO/^{13}CO intensity ratio, $\mathcal{R}$, decreases monotonically with the galactocentric radius in all mapped sources. The average $\mathcal{R}$ in the center and disk of the galaxies are 9.9±3.0 and 5.6±1.9, respectively, much lower than the peculiar $\mathcal{R}(\sim24)$ found in the center of M82. The intensity ratios of ^{13}CO/C^{18}O, ^{13}CO/HCO$^+$ and ^{13}CO/CS (either our or literature data) show little variation with galactocentric radius, in sharp contrast with the greatly varied $\mathcal{R}$. This supports the notion that the observed gradient in $\mathcal{R}$ could be the result of the variations of the physical conditions across the disks. The H$_2$ column density derived from C^{18}O shows that the Galactic standard conversion factor (X-factor) overestimates the amount of the molecular gas in M82 by a factor of ~2.5. These observations suggest that the X-factor in active star-forming regions (i.e., nuclear regions) should be lower than that in normal star-forming disks and the gradient in $\mathcal{R}$ can be used to trace the variations of the X-factor.

Key words: galaxies: ISM — ISM: clouds — ISM: molecules — radio lines: ISM

1 INTRODUCTION

It is well known that molecules constitute a significant fraction of the interstellar medium (ISM) and stars are fromed from molecular clouds. However, the most abundant molecule, H$_2$, cannot be detected directly in a typical cold (10–40 K) molecular cloud, owing to its lack of a permanent

electric dipole moment. The next most abundant molecule is ^{12}CO, which is found to be an excellent tracer of H$_2$ due to its low excitation temperature ($\sim$10 K) and critical density ($\sim$300 cm^{-3}) (Evans 1999). Generally, the lowest transition (J=1$-$0) of the rotational lines of ^{12}CO and its optically thin isotopic variants (e.g., ^{13}CO and C^{18}O) can be used to estimate the column density (N(H$_2$)) of molecular clouds in our Galaxy (Frerking et al. 1982; Young & Scoville 1982; Wilson et al. 2009). However, until now, the column density of the molecular gas in galaxies is difficult to obtain directly in this way due to the beam dilution and weakness of line emission in ^{12}CO isotopes. Accurate determination of the H$_2$ column densities from ^{12}CO observations has therefore been a longstanding challenge in external galaxies.

In our Galaxy, results from independent methods show a tight correlation between the integrated ^{12}CO line intensity $I_{^{12}CO}$ and N(H$_2$) and the ratio of N(H$_2$) to $I_{^{12}CO}$ appears to be constant with a value of (1–5)$\times$10^{20} cm^{-2} K^{-1} km^{-1} s across the Galaxy (Bohlin et al. 1978; Dickman 1978; Hunter et al. 1997; Scoville et al. 1987; Young & Scoville 1991). This constant value is denoted as the ^{12}CO-to-H$_2$ conversion factor, or the X-factor ($X \equiv N$(H$_2$)$/I_{^{12}CO}$). It is beyond the scope of this paper to analyze in great detail the origin of the empirical 'X-factor' since many studies have shown that the X-factor varies with different physical conditions and environments and which is influenced by CO abundance, gas excitation and radiative transfer processes (Scoville & Solomon 1974). For example, the amounts of molecular gas in the metal-poor Magellanic Clouds and M31 were claimed to be underestimated by up to a factor of $\sim$10 if a standard Galactic X-factor was adopted (Maloney & Black 1988; Allen & Lequeux 1993; Israel 1997). Nevertheless, recent imaging of CO clouds reports a similar standard X-factor in metal-poor galaxies (Bolatto et al. 2008). Conversely, the molecular gas contents of ultraluminous infrared galaxies (ULIRGs) might be overestimated by factors of $\sim$5 (Downes & Solomon 1998) using the standard Galactic X-factor.

The *IRAS* all-sky survey has revealed a large population of infrared bright galaxies with bulk energy emission in the far-infrared (Soifer et al. 1987; Sanders et al. 2003), which is mostly due to dust heating from starburst activity (Sanders & Mirabel 1996). Early numerous CO observations of infrared galaxies found that these galaxies are rich in molecular gas (Young et al. 1995) and there is a correlation between CO and far-infrared luminosity (Solomon & Sage 1988; Young & Scoville 1991), though the correlation is non-linear (Gao & Solomon 2004b) since L_{IR}/L_{CO} correlates with L_{IR}. Moreover, recent studies on high-redshift star forming galaxies further confirmed the validity of the CO-IR luminosity correlation (Solomon & Vanden Bout 2005; Daddi et al. 2010).

Although large quantities of observational studies have had the aim of mapping the molecular gas distribution/kinematics in nearby infrared bright galaxies with single-dish and/or interferometer telescopes (Braine et al. 1993; Young et al. 1995; Sakamoto et al. 1999; Nishiyama et al. 2001; Helfer et al. 2003; Leroy et al. 2009), these surveys are almost all based on the observations of CO J=1$-$0 or J=2$-$1 and only limited systematical studies of CO isotope variants such as ^{13}CO have been published so far (Paglione et al. 2001). Owing to the large isotope abundance ratio [^{12}CO]/[^{13}CO]$\approx$30–70 across the Galaxy (Langer & Penzias 1990), the opacity of ^{13}CO is much lower than that of ^{12}CO and thus ^{13}CO is believed to be mostly optically thin and traces the molecular gas column density adequately in most cases. Consequently, the variations in the intensity ratio of ^{12}CO to ^{13}CO as a function of galactocentric radius could give a reliable test of whether X-factor varies systematically within galaxies. Studies of the Galactic X-factor have revealed large variations in its value towards the Galactic nuclear region, with an order of magnitude increase from the center to the outer disk (Sodroski et al. 1995; Dahmen et al. 1998). In other galaxies, however, Rickard & Blitz (1985) claimed that the value of integrated intensity ratio of ^{12}CO to ^{13}CO in the nucleus is on average a factor of two higher than that in the disk. In fact, both Young & Sanders (1986) and Sage & Isbell (1991) showed that there was no clear evidence of a systematic difference in $\mathcal{R}$ within a galaxy and they suggested that the variation in $\mathcal{R}$ observed by Rickard & Blitz (1985) is likely to be caused by pointing errors. Recently, mapping surveys of ^{12}CO and ^{13}CO emission towards a large sample of nearby galaxies were carried out by Paglione et al. (2001), finding that the same physical processes

(e.g., the molecular gas kinetic temperature) may affect both $\mathcal{R}$ and X-factor, moreover, the latter is also expected to decrease from the disks to the nuclear regions by factors of 2–5.

However, any study of the physical properties of molecular gas that involves using line intensity ratios might be influenced by measurement errors, owing to the telescopes' different beam sizes, uncertain beam efficiencies, pointing errors and calibrations. Recently updated and improved sensitivity and system performance at the Purple Mountain Observatory (PMO) 14 m telescope at Delingha, China allow us to simultaneously observe extragalactic sources systematically in ^{12}CO, ^{13}CO and C^{18}O for the first time. Consequently, our simultaneous observations of three CO isotope variants with the same telescope are better suited to obtain the well-calibrated line intensity ratios than observations from different telescopes carried out with different tunings at different times.

In this paper, we present the results of simultaneous observations of ^{12}CO, ^{13}CO and C^{18}O along the major axes in nearby infrared bright galaxies. The sample selection, observations and data reduction are described in Section 2; the observed CO spectra, CO radial distributions and position-velocity diagrams are presented in Section 3. These results together with the radial distributions of molecular gas, CO isotopic ratio $\mathcal{R}$ and possible physical mechanisms that could be responsible for the observed variations in $\mathcal{R}$ are discussed in Section 4. Finally a summary is presented in Section 5. A stability analysis of the PMO 14 m telescope is presented in Appendix A.

2 SAMPLE, OBSERVATIONS AND DATA REDUCTION

The galaxies in this study were selected from the Revised Bright Galaxy Sample (RBGS, Sanders et al. 2003). We selected 11 galaxies based on the following three criteria: (1) $f_{60\mu m} \geq 50$ Jy or $f_{100\mu m} \geq 100$ Jy. This infrared flux cutoff was chosen to ensure both ^{12}CO and ^{13}CO could be detected with reasonable integration time since it is well known that the infrared luminosity of galaxies is correlated with the CO luminosity (e.g., Solomon & Sage 1988). (2) $cz \leq 1000$ km s^{-1}. This velocity limit was chosen due to the limited tuning range of the SIS receiver with the PMO 14 m telescope. (3) 9h$\leq$ R.A. $\leq$15h and Dec.$\geq$ 0°. This is because we can take full advantage of the Galactic dead time to observe galaxies in the northern sky. Some general properties of the sample galaxies are summarized in Table 1.

Table 1 Source List and Galaxy Properties

Source	Alias	R.A. (J2000.0)	Dec. (J2000.0)	V (km s^{-1})	i (°)	P.A. (°)	Type	D_{25} (arcmin)	D (Mpc)	d (kpc)
(1)	(2)	(3)	(4)	(5)	(6)	(7)	(8)	(9)	(10)	(11)
NGC 2903	UGC 5079	09 32 10.5	+21 30 05.0	556	61	17	SAB(rs)bc, HII	12.6×6.0	7.96	1.9
NGC 3031	M 81	09 55 33.6	+69 03 56.0	−34	58	157	SA(s)ab, LINER/Sy1.8	26.9×14.1	1.00	0.3
NGC 3034	M 82	09 55 49.6	+69 40 41.0	203	80^a	65^a	I0, Sbrst/HII	11.2×4.3	2.90	1.3
NGC 3521	UGC 6150	11 05 49.2	−00 02 15.0	805	58	164	SAB(rs)bc, HII/LINER	11.0×5.1	11.47	2.6
NGC 3627	M 66	11 20 15.3	+12 59 32.0	727	63	176	SAB(s)b, LINER/Sy2	9.1×4.2	10.41	2.6
NGC 3628	UGC 6350	11 20 16.2	+13 35 22.0	843	89^a	103^a	SAb pec sp, HII/LINER	14.8×3.0	12.07	3.1
NGC 4631	UGC 7865	12 42 07.1	+32 32 33.0	606	85^a	88^a	SB(s)d	15.5×2.7	8.67	2.5
NGC 4736	M 94	12 50 52.9	+41 07 15.0	308	35	100	(R)SA(r)ab, Sy2/LINER	11.2×9.1	4.40	1.4
NGC 5055	M 63	13 15 49.5	+42 01 39.0	504	55	105	SA(rs)bc, HII/LINER	12.6×7.2	7.21	2.3
NGC 5194	M 51a	13 29 53.5	+47 11 42.0	463	20^a	0	SA(s)bc pec, HII/Sy2.5	11.2×6.9	6.62	2.2
NGC 5457	M 101	14 03 09.0	+54 21 24.0	241	27	40	SAB(rs)cd	28.8×26.9	3.45	1.4

^{a} From Young et al. (1995).

Notes: Cols. (1) and (2): Galaxy name. Cols. (3) and (4): Adopted tracking center. Units of right ascension are hours, minutes, and seconds, and units of declination are degrees, arcminutes, and arcseconds. Col. (5): Heliocentric velocity drawn from the literature and NED. Cols. (6) and (7): Inclination (i) and position angle (P.A.) from Helfer et al.2003, except where noted. Col. (8): Morphological type and nuclear classification from the NED database. Col. (9): Major- and minor- axis diameters from the NED database. Col. (10): Luminosity distance, calculated assuming $H_0 = 70$ km s^{-1} MPc^{-1}. Col. (11): Linear scale of 60″ at distance D, taken from the NED database.

Our observations were made between 2008 January and 2009 December using the PMO 14 m millimeter telescope at Delingha. We used the 3mm SIS receiver operated in double-sideband mode, which allows for simultaneous observations of three CO isotope variants, with ^{12}CO in the upper sideband and ^{13}CO and C^{18}O in the lower sideband. The Half Power Beam Width (HPBW) is $\sim 60''$ and the main beam efficiency $\eta_{mb} = 0.67$. Typical system temperatures during our runs were about 180–250 K. The FFT spectrometer was used as the back end with a usable bandwidth of 1 GHz and a velocity resolution of $0.16 \, \mathrm{km \, s^{-1}}$ at 115 GHz. Observations were done in position switching mode and calibrated using the standard chopper wheel method. The absolute pointing uncertainty was estimated to be $\sim 10''$ from continuum observations of planets and the pointing was checked every two hours by taking spectra toward the standard source IRC+10216 throughout our observations. Each galaxy was first observed at the center position and then along its major axis from the center to the outer disk positions separated by half-beam size. Besides the CO observations, we also observed the dense molecular gas tracers HCO^+ and CS in the nuclear regions of galaxies.

The data were reduced using CLASS, which is part of the GILDAS[1] software package. All scans were individually inspected and those with either strongly distorted baselines or abnormal rms noise levels were discarded. Line-free channels which exhibited positive or negative spikes more than 3σ above the rms noise were blanked and substituted with values interpolated from the adjacent channels and then a linear baseline was subtracted from the 'spike-free' spectrum. After correcting each spectrum for main beam efficiency η_{mb}, the temperature scale of the spectra was converted to the main beam temperature T_{mb} scale from T_A^*. The spectra were then co-added, weighted by the inverse of their rms noises and the final spectral resolution was smoothed to $\sim 20 \, \mathrm{km \, s^{-1}}$.

Since this is the first time that the PMO 14 m millimeter telescope has systematically observed galaxies other than our own, a relatively long observing time was devoted to each pointing to accumulate adequate integration times. Thus our observations are the first long integrations of the PMO 14 m telescope ever conducted and offer an excellent opportunity to test the stability of the upgraded system (see Appendix A). The work presented here represents a total of $\sim$500 hours of observing time in CO observations before the telescope system's maintenance began in the summer of 2009 at the PMO 14m and $\sim$200 hours after the upgrade, with $\sim 40\%$ of the data being discarded due to the unstable spectrum baseline and bad weather conditions.

3 RESULTS AND ANALYSIS

3.1 CO Isotopic Spectra

We detected ^{12}CO emission from the centers of all 11 galaxies observed, of which 10 were also detected in ^{13}CO simultaneously. Four galaxies (NGC 3627, NGC 3628, NGC 4631 and M51) were observed along the major axes, and ^{12}CO emission was detected at all 42 off-center positions along the major axes, while ^{13}CO was detected at 27 out of the 42 positions. For M82, the starburst galaxy, ^{12}CO emission was detected at all 47 positions that were mapped in the central $4' \times 2.5'$ region, while ^{13}CO was tentatively detected at 15 positions. C^{18}O emission was only detected at 13 points close to the nuclear regions in M51 and M82.

Here, we focus on presenting ^{13}CO and C^{18}O spectra as compared to ^{12}CO observed simultaneously at the same positions. ^{12}CO spectra at those ^{13}CO undetected positions are not shown here, since many previous observations of ^{12}CO emission in these galaxies are available in literature (e.g., Young et al. 1995) and our ^{12}CO observations show similar results and comparable spectra. The spectra of both ^{12}CO and ^{13}CO, as well as *Spitzer* IRAC 3.6 μm, 8 μm and MIPS 24 μm infrared composite color images showing the observed beam positions of the mapped galaxies, are shown in Figure 1. All the three CO isotopic spectra at those C^{18}O detected positions are shown in Figure 2.

---

[1] *http://iram.fr/IRAMFR/GILDAS/*
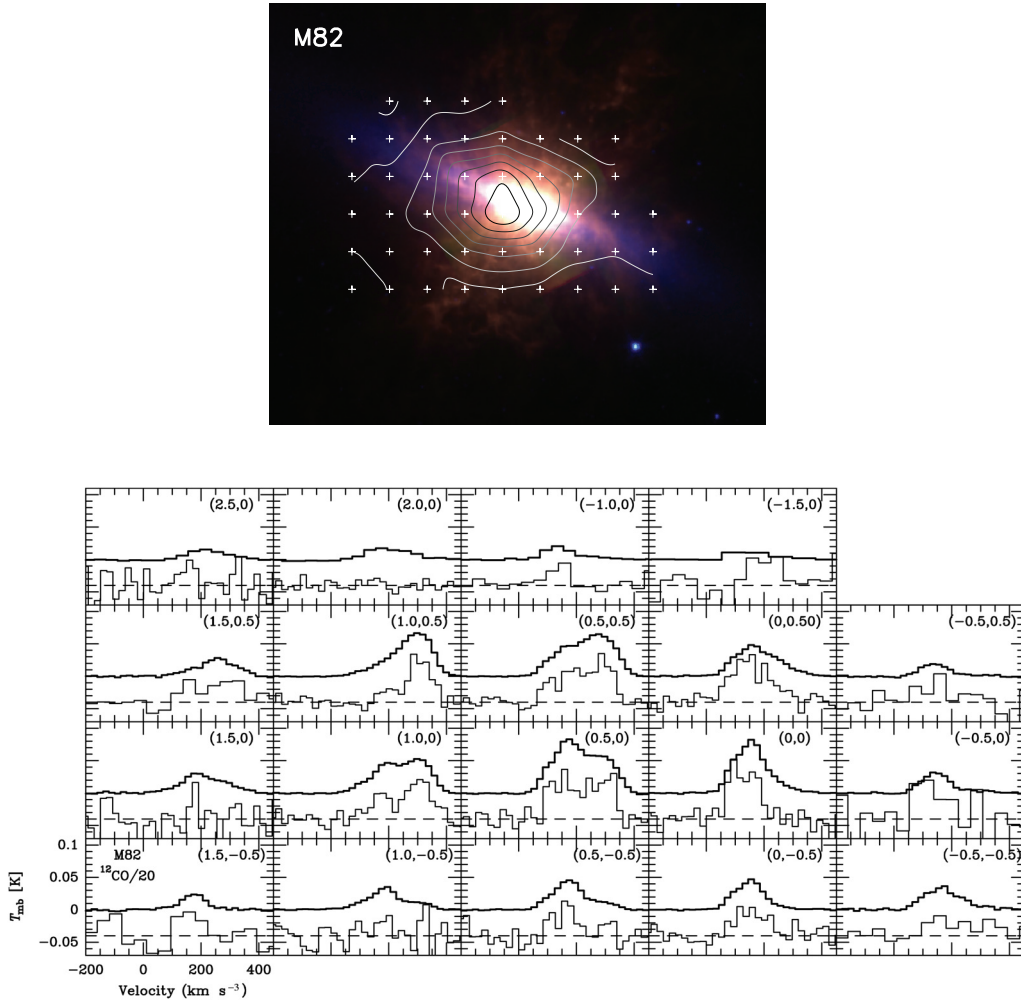
Fig. 1(a) Spectra of ^{12}CO (*thick lines*) and ^{13}CO (*thin lines*) from the central region of M82 with ^{13}CO tentatively detected. All spectra are on the $T_{\rm mb}$ scale and binned to a velocity resolution of $\sim$20 km s^{-1} (for some weak ^{13}CO emission positions, the spectra are further smoothed to $\sim$40 km s^{-1} for display). ^{12}CO spectra are divided by 20 for comparison purposes. The offset from the center position is indicated in each box. A linear baseline has been subtracted using the line-free portions of each spectrum. M82 was mapped in the $4' \times 2.5'$ central region. The top panel shows the observed positions (crosses) and ^{12}CO contours (contours begin at 10 K km s^{-1} and increase by 40 K km s^{-1} at each step) overlaid on an infrared image taken from *Spitzer* (8.0 μm (*red*), 5.8 μm (*green*), 3.6 μm (*blue*)).

3.2 Derived Parameters

The observation results and derived properties are summarized in Table 2. The velocity-integrated ^{12}CO (and isotopes) intensity, $I_{\rm CO} \equiv \int T_{\rm mb}dv$, is obtained by integrating $T_{\rm mb}$ over the velocity range of the CO line emission feature. Using the standard error formulae in Gao (1996) (also in
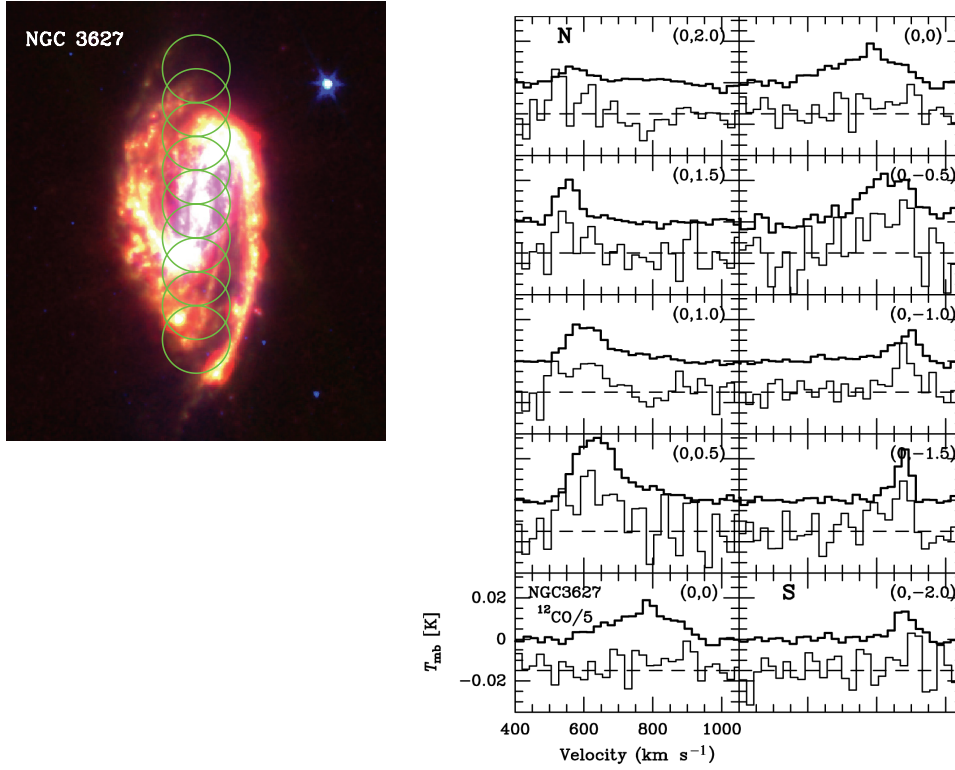
Fig. 1(b) Same as Fig. 1(a), but for NGC 3627. The spectra were measured along the major axis (PA=176°) of the galactic disk. The left panel shows the half-beam-spaced observations overlaid on a *Spitzer* infrared image (24.0μm (*red*), 8.0μm (*green*), 3.6μm (*blue*)). The size of HPBW ($\sim 60''$) is represented by a circle.

Matthews & Gao 2001), the error in the integrated intensity is

$$\Delta I = T_{\rm rms}\,\Delta v_{\rm FWZI}/[f\,(1 - \Delta v_{\rm FWZI}/W)]^{1/2}\ [{\rm K\ km\ s^{-1}}], \tag{1}$$

where $T_{\rm rms}$ is the rms noise in the final spectrum in mK, $f = \Delta v_{\rm FWZI}/\delta_v$, where $\Delta v_{\rm FWZI}$ is the linewidth of the emission feature, δ_v is the channel bin spacing, and W is the entire velocity coverage of the spectrum in units of kilometers per second. For non-detections (only CO isotopes), some spectra are further smoothed and found to be marginally detected with signal-to-noise of $\sim$2.5. Otherwise, $2\sigma_I$ upper limits are given based on estimates by using the expected line width from the detected ^{12}CO lines at exactly the same position.

The H$_2$ column density and mass surface density for galaxies in our sample are derived from the empirical relations (Nishiyama et al. 2001)

$$N({\rm H_2})[{\rm cm^{-2}}] = 2 \times 10^{20} I_{^{12}{\rm CO}}[{\rm K\ km\ s^{-1}}], \tag{2}$$

and

$$\Sigma({\rm H_2})[M_\odot {\rm pc^{-2}}] = 3.2 I_{^{12}{\rm CO}}[{\rm K\ km\ s^{-1}}]\cos i, \tag{3}$$

where $\cos i$ corrects the mass to face-on and a Galactic ^{12}CO-to-H$_2$ conversion factor $X = 2.0\times10^{20}$ cm^{-2} K^{-1} km^{-1} s is adopted (Dame et al. 2001). It can obviously be seen from Table 2

Table 2 Observed and Derived Properties of ^{12}CO and ^{13}CO

Source	$\Delta\alpha^a$ (′)	$\Delta\delta^a$ (′)	^{12}CO $I_{^{12}\mathrm{CO}} \pm \sigma_I{}^b$ (K km s^{-1})	V^c_{mean} (km s^{-1})	ΔV^c	^{13}CO $I_{^{12}\mathrm{CO}} \pm \sigma_I^b$ (K km s^{-1})	V^c_{mean} (km s^{-1})	ΔV^c	$\mathcal{R}^d$	$\tau(^{13}\mathrm{CO})^e$	$N(\mathrm{H}_2)^f$ (10^{20}cm^{-2})	T_k^g (K)
(1)	(2)	(3)	(4)	(5)	(6)	(7)	(8)	(9)	(10)	(11)	(12)	(13)
NGC 2903	0.00	0.00	24.89±0.92	548	155	1.95±0.58	591	151	12.8±4.3	0.08	49.8	55
NGC 3031	0.00	0.00	0.66±0.28	−38	127	< 0.68	...	...	>1.0	...	1.3	...
M82	0.00	0.00	224.61±1.51	159	138	10.25±0.82	126	123	21.9±1.9	0.05	449.2	98
	0.00	0.50	163.0±1.62	180	162	11.80±1.06	153	167	13.8±1.4	0.08	328.8	66
	0.00	−0.50	113.4±1.12	150	115	5.59±0.90	137	150	20.3±3.5	0.05	230.0	110
	0.50	0.00	344.77±2.04	214	184	13.91±1.31	230	194	24.8±2.5	0.04	689.5	111
	0.50	0.50	278.07±1.53	233	183	11.37±0.97	238	180	24.5±2.2	0.04	556.1	110
	0.50	−0.50	134.00±1.50	169	125	5.61±1.10	162	87	23.9±4.9	0.04	269.8	110
	1.00	0.00	228.83±1.66	242	180	11.29±1.25	265	142	20.3±2.4	0.05	457.7	90
	1.00	0.50	218.00±1.69	268	162	6.38±0.83	313	110	34.2±4.7	0.03	435.8	120
	1.50	0.50	92.34±2.04	255	164	6.99±1.01	264	215	13.2±2.2	0.08	184.7	57
	1.50	−0.50	48.95±1.74	173	94	3.64±1.36	158	82	13.4±5.5	0.08	97.9	58
	2.50	0.00	48.64±2.44	219	147	1.94±0.96	158	46	25.1±13.7	0.04	97.3	113
	−0.50	0.00	75.91±1.88	144	112	6.78±2.83	114	100	11.2±5.0	0.09	151.8	48
	−0.50	−0.50	45.75±1.66	140	110	5.75±1.33	226	250	7.9±2.1	0.13	91.5	32
	−1.00	0.00	47.85±1.96	135	104	2.52±1.49	141	44	18.9±12.0	0.05	95.7	84
	−1.50	0.00	47.40±3.86	162	147	5.81±2.16	183	111	8.2±3.7	0.13	94.8	33
NGC 3521	0.00	0.00	22.00±0.37	770	231	2.05±0.66	770	210	10.7±3.7	0.10	44.0	45
NGC 3627	0.00	0.00	17.24±0.87	769	179	1.66±0.49	866	200	10.4±3.6	0.10	34.5	44
	0.00	0.50	25.26±0.83	653	157	4.06±0.98	625	163	6.2±1.7	0.18	50.5	24
	0.00	1.00	13.88±0.38	633	177	2.28±0.51	597	138	6.1±1.5	0.18	27.8	23
	0.00	1.50	8.55±0.52	554	58	1.46±0.48	580	75	5.9±2.3	0.19	17.1	22
	0.00	2.00	6.90±0.50	583	75	1.79±0.35	527	74	3.9±1.0	0.30	13.8	13
	0.00	−0.50	22.25±1.96	827	115	2.87±0.69	829	145	7.7±2.5	0.14	44.5	31
	0.00	−1.00	8.96±0.53	851	185	1.78±0.35	885	91	5.0±1.3	0.22	17.9	18
	0.00	−1.50	6.82±0.31	872	56	1.96±0.41	877	90	3.5±0.9	0.34	13.6	11
	0.00	−2.00	5.90±0.42	886	66	1.02±0.40	902	43	5.1±2.5	0.19	11.8	22
NGC 3628	0.00	0.00	35.80±0.67	823	232	3.22±0.50	839	211	11.1±1.9	0.09	71.6	47
	0.49	−0.11	28.95±0.52	865	204	<2.52	...	...	>11.5	...	57.9	...
	0.98	−0.22	9.95±0.77	962	150	2.52±0.60	986	110	3.9±1.2	0.29	19.9	13
	1.96	−0.44	3.77±0.92	998	88	<1.76	...	...	>2.1	...	7.5	...
	2.94	−0.66	2.13±0.64	1030	72	<1.18	...	...	>1.8	...	4.3	...
	−0.49	0.11	14.06±0.46	751	177	3.07±0.49	745	206	4.6±0.9	0.25	28.1	16
	−0.98	0.22	16.16±1.47	738	113	<2.04	...	...	>7.9	...	32.3	...
	−1.96	0.44	6.45±0.81	658	130	1.35±0.48	675	83	4.8±2.3	0.23	12.9	17
	−2.94	0.66	2.95±1.11	636	64	<2.22	...	...	>1.3	...	5.9	...
NGC 4631	0.00	0.00	17.36±0.62	623	144	1.65±0.46	606	146	10.5±3.3	0.10	34.7	44
	0.51	0.02	23.77±0.24	674	93	2.53±0.46	677	80	9.4±1.8	0.11	47.5	39
	1.00	0.03	13.82±0.67	673	152	1.48±0.42	697	198	9.3±3.0	0.11	27.6	39
	1.50	0.06	4.98±0.26	726	102	0.71±0.27	704	108	7.0±3.0	0.15	9.9	28
	2.00	0.06	4.07±0.25	715	112	1.25±0.21	731	148	3.3±0.7	0.37	8.1	10
	2.50	0.11	3.29±0.19	718	90	<0.52	...	...	>6.3	...	6.6	...
	2.99	0.22	2.48±0.33	739	70	<0.80	...	...	>3.1	...	5.0	...
	−0.51	−0.02	19.50±0.27	571	105	1.76±0.31	528	141	11.1±2.1	0.09	39.0	47
	−1.00	−0.03	11.40±0.44	590	146	1.77±0.47	600	140	6.4±1.9	0.17	22.8	25
	−1.50	−0.06	3.41±0.23	524	99	<0.83	...	...	>4.0	...	6.8	...
	−2.00	−0.07	1.89±0.16	529	108	<0.52	...	...	>3.6	...	3.8	...
	−2.50	−0.11	1.96±0.14	535	83	<0.40	...	...	>4.9	...	3.9	...
	−2.99	−0.22	2.20±0.31	526	76	<0.90	...	...	>2.4	...	4.4	...

Table 2 — *Continued.*

Source	$\Delta\alpha^a$ (′)	$\Delta\delta^a$ (′)	^{12}CO $I_{^{12}\mathrm{CO}} \pm \sigma_I{}^b$ (K km s^{-1})	V^c_{mean} (km s^{-1})	ΔV^c	^{13}CO $I_{^{12}\mathrm{CO}} \pm \sigma_I^b$ (K km s^{-1})	V^c_{mean} (km s^{-1})	ΔV^c	$\mathcal{R}^d$	$\tau(^{13}\mathrm{CO})^e$	$N(\mathrm{H}_2)^f$ (10^{20} cm^{-2})	T^g_k (K)
(1)	(2)	(3)	(4)	(5)	(6)	(7)	(8)	(9)	(10)	(11)	(12)	(13)
	−3.50	−0.38	2.86±0.19	521	51	<1.10	...	...	>2.6	...	5.7	...
	−3.68	−0.30	3.68±0.30	510	43	0.71±0.25	486	34	5.2±2.2	0.21	7.4	19
NGC 4736	0.00	0.00	8.01±0.70	340	153	1.12±0.29	391	114	7.2±2.5	0.15	16.0	28
NGC 5055	0.00	0.00	16.15±1.05	527	214	2.09±0.86	527	275	7.7±3.7	0.14	32.3	31
M51	0.00	0.00	33.35±0.39	475	103	3.86±0.35	472	87	8.6±0.9	0.12	66.7	35
	0.00	0.50	28.90±0.42	434	80	3.01±0.48	425	37	9.6±1.7	0.11	57.8	40
	0.00	1.00	17.45±0.56	410	30	2.43±0.41	408	23	7.2±1.4	0.15	34.9	29
	0.00	1.50	10.35±0.50	406	30	1.26±0.41	409	41	8.2±3.1	0.13	20.7	34
	0.00	2.00	9.70±0.45	401	32	1.98±0.59	406	26	4.9±1.7	0.23	19.4	18
	0.00	2.50	6.90±0.37	398	29	0.80±0.29	396	37	8.6±3.5	0.12	13.8	36
	0.00	3.00	2.62±0.56	388	20	<1.00	...	...	>2.6	...	5.2	...
	0.00	−0.50	27.35±0.53	513	62	2.28±0.49	520	58	12.0±2.8	0.09	54.7	51
	0.00	−1.00	16.25±0.55	534	49	1.90±0.44	536	42	8.5±2.3	0.12	32.5	35
	0.00	−1.50	6.55±0.23	534	51	0.86±0.22	563	53	7.6±2.2	0.14	13.1	31
	0.00	−2.00	7.90±0.37	538	36	1.64±0.38	539	43	4.8±1.3	0.23	15.8	17
	0.00	−2.50	5.77±0.33	534	46	<0.68	...	...	>8.5	...	11.5	...
	0.00	−3.00	2.28±0.35	553	36	<0.62	...	...	>3.7	...	4.6	...
M51 disk^h	...	...	11.85±0.30	462	151	1.73±0.37	411	20	6.8±1.6	0.16	23.7	27
NGC 5457	0.00	0.00	9.82±0.51	255	72	1.97±0.49	277	128	5.0±1.5	0.22	19.6	18

^{a} Offsets from the nucleus position listed in Table 1, in units of arcminutes.

^{b} The measured integrated intensities and associated uncertainties, calculated using the prescription explained in the text. For non-detections, a $2\sigma_I$ upper limit was given.

^{c} Velocity and line width are either Gaussian-fitted values or are calculated from the moment for non-Gaussian lines.

^{d} The ratio of ^{12}CO to ^{13}CO integrated intensities. The errors are based on the statistical uncertainties of integrated intensities, which can be derived from the error transfer formula $\sigma(\mathcal{R}_{12/13}) = \left(\left[\frac{\sigma(I_{12})}{I_{13}} \right]^2 + \left[\frac{\sigma(I_{13}) \times \mathcal{R}_{12/13}}{I_{13}} \right]^2 \right)^{1/2}$.

^{e} The average optical depth of the ^{13}CO emission line, calculated from Equation (4).

^{f} H$_2$ column density calculated from ^{12}CO data by adopting Galactic standard X-factor, 2.0×10^{20} cm^{-2} K^{-1} km^{-1} s.

^{g} The gas kinetic temperature calculated from the assumption of LTE conditions by equating the column densities derived from both ^{12}CO and ^{13}CO (see text Section 3.2).

^{h} M51 disk represents the average intensity over the disk region except for the nucleus.

that the column density in M82 is generally one order of magnitude higher than that in normal spiral galaxies (the rest of the sample).

Assuming that ^{13}CO has the same excitation temperature as ^{12}CO and the molecular cloud is under local thermal equilibrium (LTE) conditions, then we can calculate the average ^{13}CO optical depth from

$$\tau(^{13}\mathrm{CO}) = \ln \left[1 - \frac{\int T^*_{\mathrm{R}}(^{13}\mathrm{CO})dv}{\int T^*_{\mathrm{R}}(^{12}\mathrm{CO})dv} \right]^{-1}, \tag{4}$$

where T^*_{R} should be corrected for the filling factor, so here we can only estimate an average over all of the unresolved clouds in the beam. Using the definition in Wilson et al. (2009), the H$_2$ column density can be derived from the ^{13}CO line intensity as

$$N(\mathrm{H}_2)(^{13}\mathrm{CO}) = \left[\frac{\tau(^{13}\mathrm{CO})}{1 - \mathrm{e}^{-\tau(^{13}\mathrm{CO})}} \right] 2.25 \times 10^{20} \frac{\int T_{\mathrm{mb}}(^{13}\mathrm{CO})dv}{1 - \mathrm{e}^{-5.29/T_{\mathrm{ex}}}}, \tag{5}$$
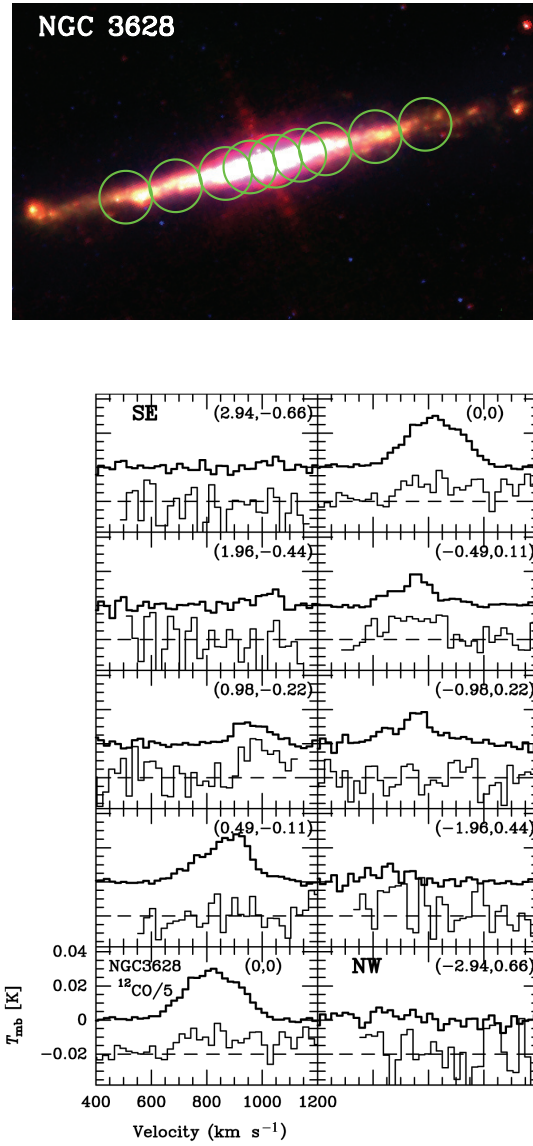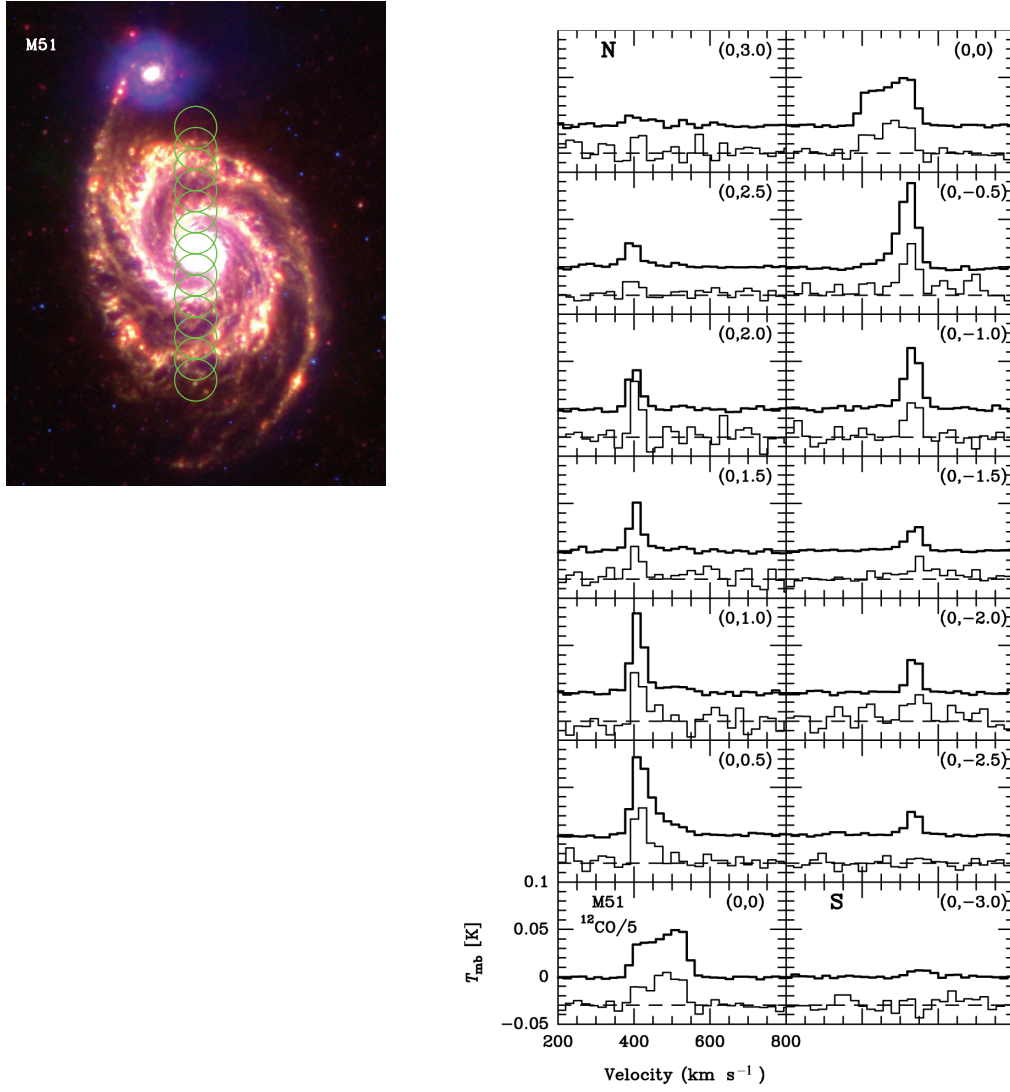
Fig. 1(c) Same as Fig. 1(b), but for NGC 3628. The spectra were measured along the major axis (PA=103°) of the galactic disk.

where the ^{13}CO abundance [^{13}CO]/[H$_2$] is 8×10^{-5}/60 (Frerking et al. 1982) and the excitation temperature, T_{ex}, is taken to be the kinetic temperature of the gas, T_K. Thus, we can estimate T_K by equating the column densities derived from both ^{12}CO and ^{13}CO. Both the derived $\tau(^{13}$CO) and T_K are listed in Table 2. Note that the LTE assumption is most likely invalid in the central regions of M82. Thus, the extremely low optical depth of ^{13}CO ($\sim$0.04) should be treated only as a lower limit and the resulting kinetic temperature (between 70 and 120 K), which is about 3–4 times higher than that in normal galaxies, should be treated as an upper limit.
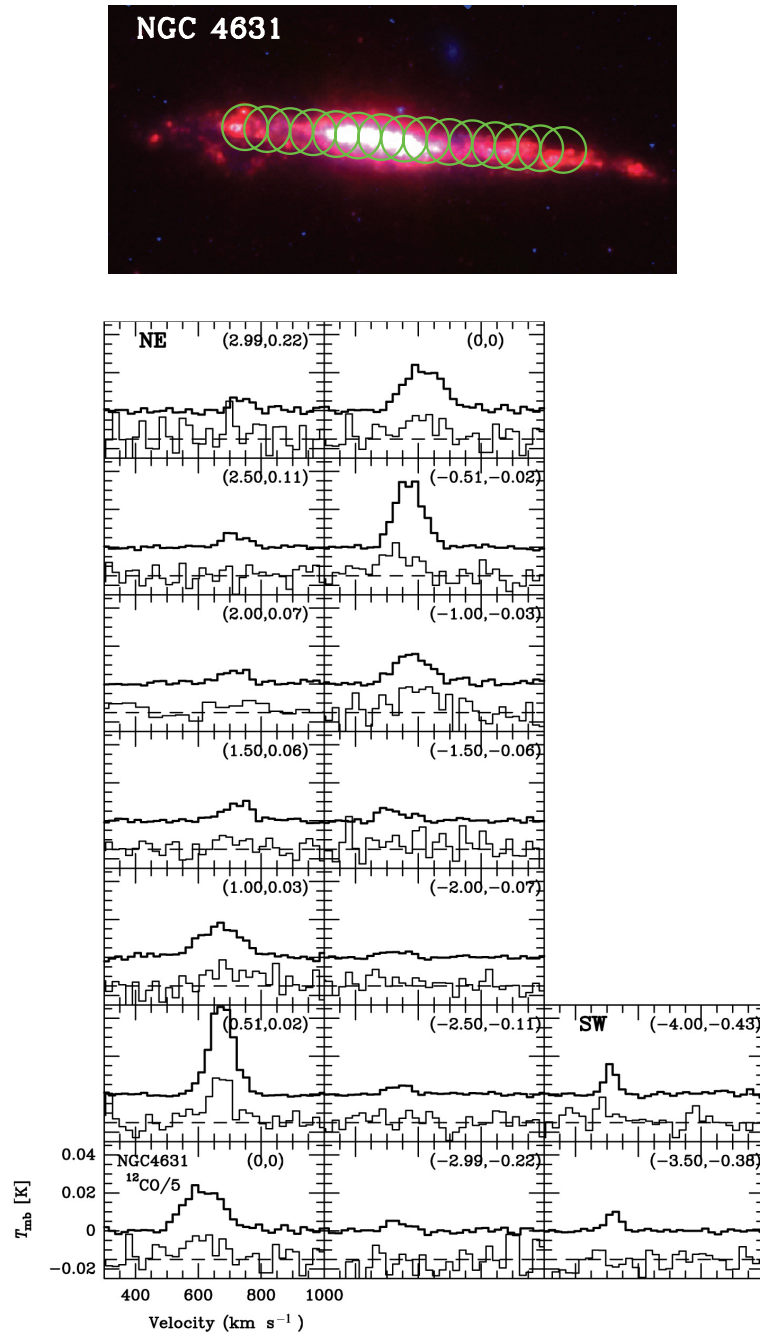
Fig. 1(d) Same as Fig. 1(b), but for NGC 4631. The spectra were measured along the major axis (PA=88°) of the galactic disk.

Fig. 1(e) Same as Fig. 1(b), but for M51. The spectra were measured along the major axis (PA=0°) of the galactic disk.

Similarly, we estimated the optical depth of C^{18}O adopting the same method as Equation (4) and derived the H$_2$ column density from C^{18}O intensity using (Sato et al. 1994)

$$N(H_2)(C^{18}O) = \left[\frac{\tau(^{18}CO)}{1 - e^{-\tau(^{18}CO)}} \right] 1.57 \times 10^{21} \frac{\int T_{mb}(C^{18}O)dv}{1 - e^{-5.27/T_{ex}}}, \qquad (6)$$

where the abundance of [C^{18}O]/[H$_2$] is 1.7×10^{-7} (Frerking et al. 1982) and T_{ex} is adopted from the value listed in Table 2. The derived values of $\tau(C^{18}O)$ and $N(H_2)(C^{18}O)$ for the 13 points of M82 and M51 detected in C^{18}O are listed in Table 3. The average optical depths of C^{18}O in
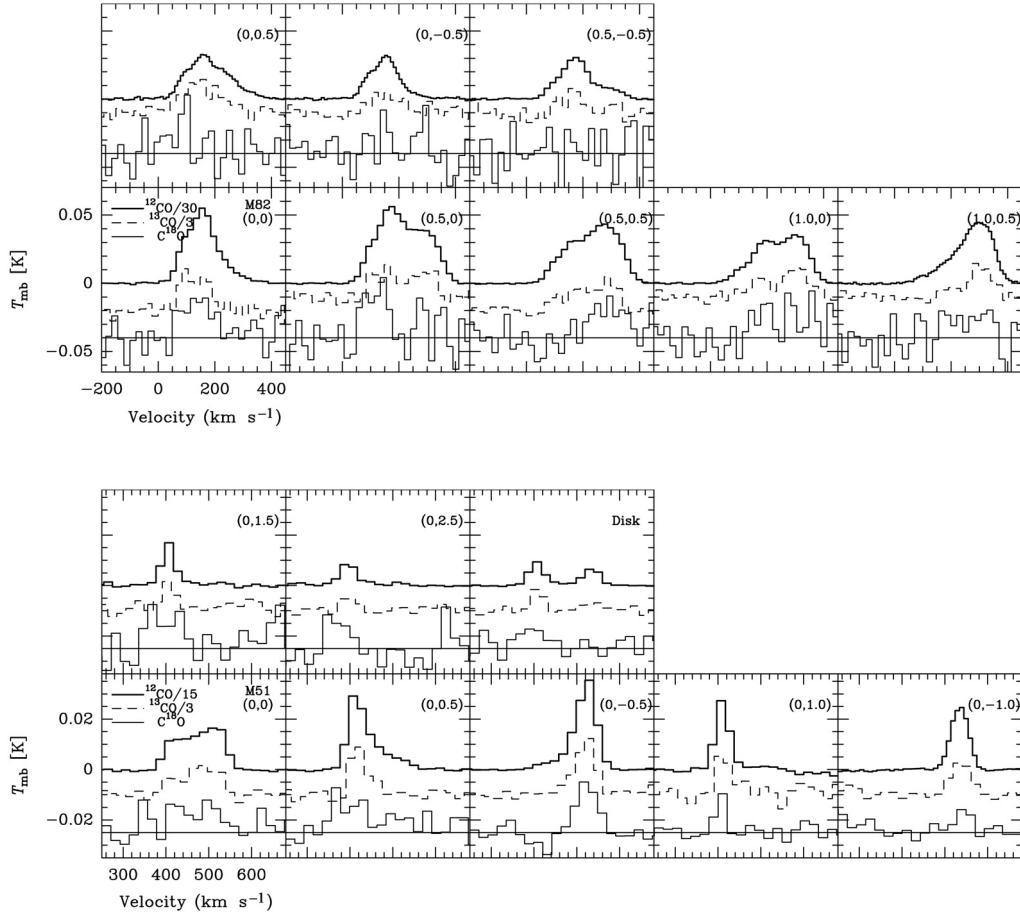
**Fig. 2** Spectra of ^{12}CO, ^{13}CO and C^{18}O obtained from the same positions on the galaxy M82 and M51. ^{12}CO spectra are divided by 30 and 15 for display in M82 and M51, respectively, while ^{13}CO spectra are divided by 3 for display. M51 disk spectra represent the average emission over the disk region except for the center (0,0).

M82 and M51 are 0.02 and 0.05, respectively; both are about three times lower than that of ^{13}CO. Therefore, although the optical depth of ^{13}CO is moderate ($\tau(^{13}$CO$) \sim 0.3$–0.4) in a few galaxies (e.g., NGC 3627 and NGC 4631; see Table 2), C^{18}O is always optically thin in all cases here.

3.3 Distribution of CO Isotopes and Line Ratios

The distributions of ^{12}CO and ^{13}CO velocity-integrated intensities and their ratio $\mathcal{R}$ as a function of galacto-central radius are shown in Figure 3. Note that none of these profiles have been corrected for inclination. Both the ^{12}CO and ^{13}CO emission line intensities show an exponential decrease with radius and the ratio $\mathcal{R}$ decreases from nucleus to the outer disk.
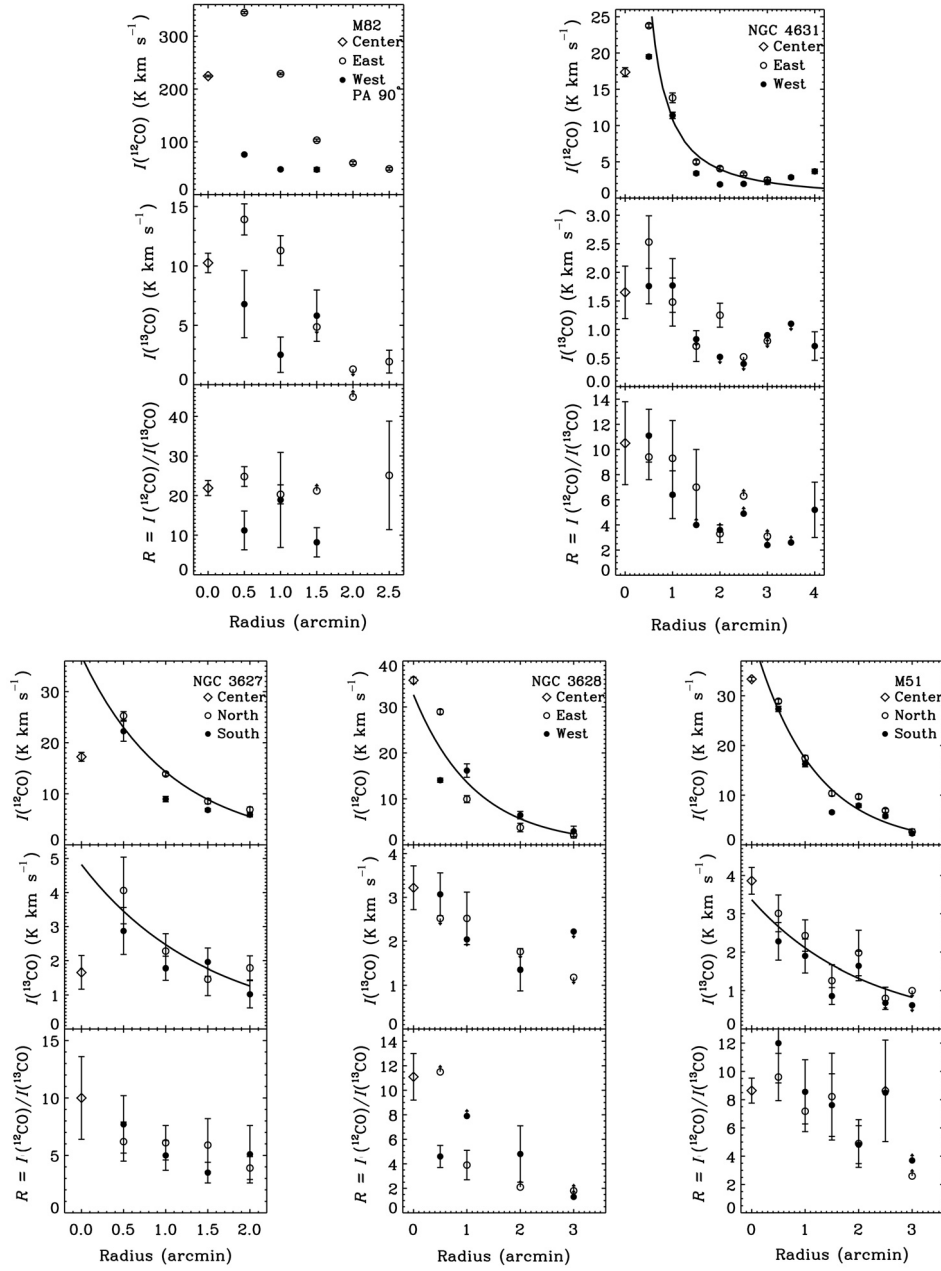
Fig. 3 Radial distributions of ^{12}CO and ^{13}CO integrated intensity and their ratios at each position along the major axes (for M82, the distributions along the axis with position angle of 90° are shown). Error bars are 1σ statistical uncertainty based on the measured rms noise in each spectrum. Upper limits (2σ) are denoted with a downward arrow for the non-detection of ^{13}CO emission; the corresponding lower limits of line ratio $\mathcal{R}$ are denoted with an upward arrow. The solid lines in NGC 3627 and M51 represent the exponential fit to the radial distribution of mean intensity of ^{12}CO and ^{13}CO emission, while the ones in NGC 4631 and NGC 3628 represent the power-law fit to ^{12}CO emission.

Table 3 Observed and Derived Properties of $C^{18}O$

Source	$\Delta\alpha$ (′)	$\Delta\delta$ (′)	$I_{C^{18}O} \pm \sigma_I$ (K km s^{-1})	V_{mean} (km s^{-1})	ΔV (km s^{-1})	$\tau(C^{18}O)^a$	$N(H_2)^b$ (10^{21} cm^{-2})
(1)	(2)	(3)	(4)	(5)	(6)	(7)	(8)
M82	0.0	0.0	3.81±0.90	140	121	0.017	18.6
	0.0	0.5	<4.2	...	...	...	...
	0.0	−0.5	2.55±1.27	224	176	0.022	14.0
	0.5	0.0	3.80±0.90	145	93	0.011	25.2
	0.5	0.5	3.30±0.76	289	135	0.012	20.5
	0.5	−0.5	<4.1	...	...	...	...
	1.0	0.0	4.19±1.20	284	236	0.018	20.6
	1.0	0.5	3.14±1.84	256	174	0.015	14.8
M51	0.0	0.0	1.04±0.35	466	176	0.032	7.4
	0.0	0.5	0.92±0.49	413	154	0.032	5.7
	0.0	1.0	0.45±0.16	407	23	0.026	4.6
	0.0	1.5	0.99±0.54	393	79	0.10	2.4
	0.0	2.0	<1.17	...	...	...	...
	0.0	2.5	0.88±0.37	369	58	0.14	1.6
	0.0	−0.5	0.95±0.17	519	37	0.035	4.3
	0.0	−1.0	0.55±0.13	544	35	0.034	3.6
	0.0	−1.5	<0.68	...	...	...	...
	0.0	−2.0	<0.84	...	...	...	...

[a] The average optical depth in the $C^{18}O$ emission line is calculated from a similar equation as Equation (4).
[b] H_2 column density derived from $C^{18}O$, calculated from Equation (6).

3.3.1 Radial distributions of ^{12}CO and ^{13}CO

The obvious trends shown in Figure 3 are that the observed radial distribution of ^{13}CO follows that of ^{12}CO. The integrated line intensities usually peak in the center of galaxies and fall monotonically toward larger galactocentric radii. For the barred spiral galaxies NGC 3627 and NGC 4631, however, both ^{12}CO and ^{13}CO intensities peak at a radius of ~ 1 kpc ($\sim 0.5'$) rather than at the nuclei. The same feature has also been presented in Paglione et al. (2001) for NGC 4631. Some previous high resolution observations of barred galaxies revealed that the molecular gas was concentrated in the central regions, with secondary peaks at the bar ends due to the bar potential and the viscosity of the gas (Regan et al. 1999; Sakamoto et al. 1999).

Similar to the stellar luminosity profiles, the observed ^{12}CO radial distributions in NGC 3627, NGC 3628 and M51 could also be well fitted by an exponential fit in R

$$I(R) = I_0 \exp\left(-R/R_0\right), \tag{7}$$

where R is the galactocentric distance, R_0 is the disk scale length and I_0 is the central integrated intensity. The solid curves in Figure 3 show the least-squares fit to the data excluding the center point since the nuclear gas could be a distinct component, yielding $I_0 = 32.6$ K km s^{-1} and $R_0 = 3.5$ kpc for the ^{12}CO emission in NGC 3628, and $I_0 = 37.8$ K km s^{-1} and $R_0 = 2.7$ kpc, and $I_0 = 3.5$ K km s^{-1} and $R_0 = 3.8$ kpc for ^{12}CO and ^{13}CO emission in M51, respectively. In NGC 3627, the scale lengths are 2.8 kpc and 3.9 kpc for the ^{12}CO and ^{13}CO emission, respectively. However, the power-law fit with a functional form, $I = I_0 R^\alpha$, is more suitable than any exponential fit for the ^{12}CO distribution in NGC 4631. The fit result gives $\alpha = -1.5$ and $I_0 = 41.1$ K km s^{-1}. For the other three exponentially-fit galaxies, the power-law could also fit the ^{12}CO distribution almost equally well. The exponential ^{12}CO scale lengths of 2–4 kpc equal $\sim 0.2\, R_{25}$, which is consistent with the results in Nishiyama et al. (2001). The distributions of ^{12}CO and ^{13}CO emission along the axis with position angle of 90° in M82 are similar to the other four galaxies. The distributions along

the major axis are not shown here, since the observations of M82 were carried out by mapping an area of $4' \times 2.5'$.

3.3.2 The integrated line intensity ratios

The intensity ratio $\mathcal{R}$ ranges from 3.3±0.7 to 12.8±4.3 for all 36 points detected in both ^{12}CO and ^{13}CO emission from normal spiral galaxies, with mean values of 9.9±3.0 and 5.6±1.9 for the central and disk regions, respectively. However, the average $\mathcal{R}$ in M82 is about 2.5 times higher than that in the nucleus of normal spiral galaxies. We use equation (2) in Young & Sanders (1986) to calculate the mean value of $\mathcal{R}$ at each radius. The most prevalent trend is that the $\mathcal{R}$ drops at larger radii in both the barred and non-barred spiral galaxies that we have mapped along the major axis in our sample (Fig. 3). Here we note that two points ($\sim$2.5$'$ away from the center) are found to have significantly higher ratios ($\sim$9) in M51. These abnormally high values in the disks tend to be observed once the telescope beams are located in the most active star-forming regions along spiral arms.

The detection of C^{18}O in M82 and M51 also allows us to estimate the intensity ratio of ^{13}CO to C^{18}O, which ranges between 0.9±0.7 and 5.3±2.8 with mean value of 2.9±1.4. The ratios measured in the nucleus and disk of M51 are 3.7 and 2.6, respectively. These values agree well with the results of Vila-Vilaró (2008), who claimed to first detect C^{18}O emission in the center of M51 with a ^{13}CO/C^{18}O ratio of 3.6. Also, similar ^{13}CO/C^{18}O ratio values have been found in some starburst galaxies (e.g., Sage et al. 1991; Aalto et al. 1995). In addition, our detection of C^{18}O in the off-center regions of M51 represents the first report of such detection for this object so far.

Ongoing observations of emission lines HCO$^+$ and CS, which are the tracers of dense molecular gas towards the nuclear regions of NGC 4736, M82, NGC 3628 and M51 have so far only yielded detection in the latter three galaxies. Here, we also use these limited dense gas observations, along with the literature data of dense gas observations, to help further analyze the CO isotopic results. The intensity ratios of ^{13}CO to HCO$^+$ and ^{13}CO to CS are found to show little variation between starburst and normal galaxies, with average values of 1.3±0.3 and 3.2±1.4, respectively. The observed integrated intensity and line ratios and the literature data used are listed in Table 3.

3.4 Kinematics of CO

Figure 4 shows the CO position-velocity ($P - V$) diagrams along the major axes of the galaxies NGC 3627, NGC 3628, NGC 4631 and M51, and the $P - V$ diagrams with position angles of 0° and 90° in M82 as well. It can be seen in Figure 4 that $P - V$ diagrams along the major axes tend to show a gradual increase of rotation velocity in the inner regions (rigid rotation) and a nearly constant velocity in the outer regions (differential rotation).

For NGC 3627 and M51, the $P - V$ spatial velocity maps of ^{13}CO are also shown in Figure 4. Obviously, both ^{12}CO and ^{13}CO show essentially similar kinematics and distributional characteristics. At each position where observations were made, the distribution of line intensity and the velocity range for ^{12}CO and ^{13}CO emission are in good agreement. Accordingly, it could also indicate that the line ratios at each position derived from our observations are reliable.

Figure 5 shows the CO rotation curve and the variation in line width along the major axis. Using the mean velocity, inclination, systemic velocity and position angle of the major axis that are listed in Table 1, and by the assumption that the observed velocity reflects only the systemic motion of the whole galaxy and circular rotation, the rotation velocity V_{R} can be derived via

$$V_{\mathrm{R}} = (V_{\mathrm{obs}} - V_{\mathrm{sys}})/\sin i \, \cos\theta \,, \tag{8}$$

where V_{obs} is an observed velocity of ^{12}CO, V_{sys} is the systemic velocity of the galaxy, i is the inclination angle and θ is the azimuth measured in the disk plane. The peak velocity, V_{max}, in the
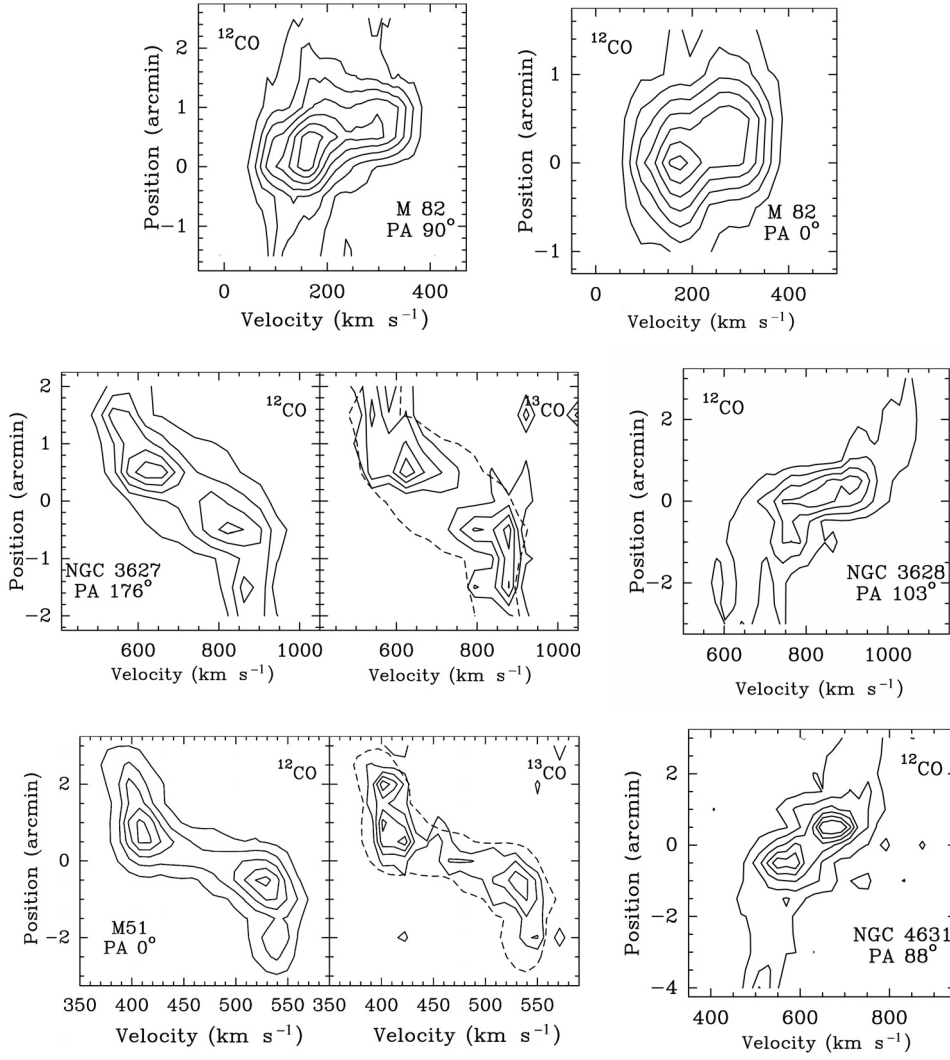
Fig. 4 Position-velocity diagram of ^{12}CO and ^{13}CO (only for NGC 3627 and M51) emission along the major axes of galaxies. For M82, the $P - V$ diagrams with position angles of $0°$ and $90°$ are shown. All the spectra were smoothed to have a velocity resolution of $\sim 20\,\mathrm{km\,s^{-1}}$. The dashed contour on the ^{13}CO panel represents the lowest ^{12}CO contour for comparison.

rotation curve of our sample galaxies, ranges from 120 to 240 km s^{-1} (V_{max} values in spiral galaxies are usually between 150 and 300 km s^{-1}, Sparke & Gallagher 2000).

4 DISCUSSION

4.1 Radial Distribution of Molecular Gas

In Section 3.3, we show that the surface density of the molecular gas in the galaxies observed in our sample can be well fitted both by an exponential and a power-law function. The χ^2 values indicate
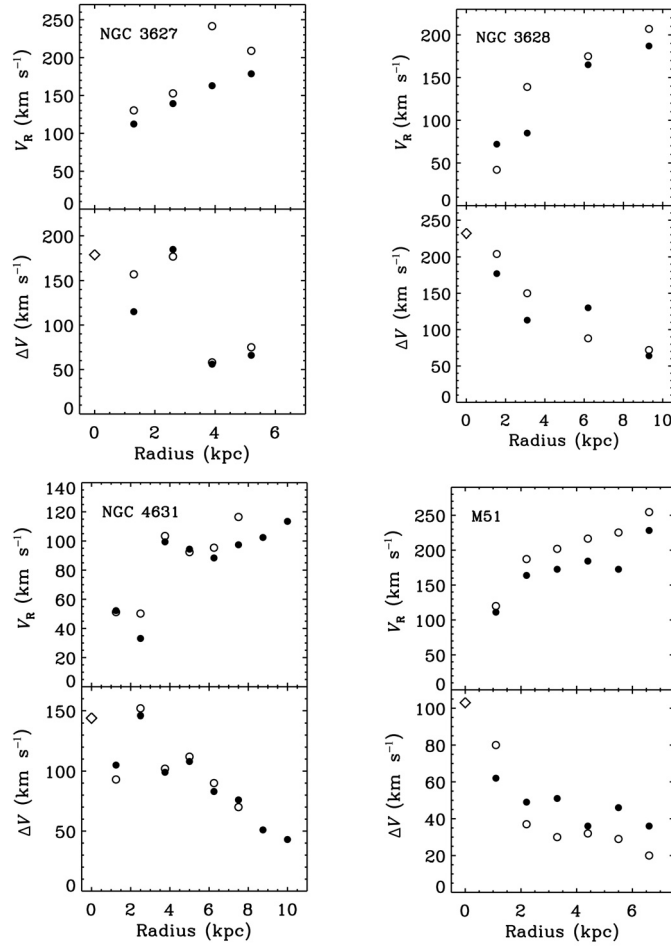
Fig. 5 Rotation velocity derived from the ^{12}CO emission line using Equation (8) and line width measured at each position along the major axis. The different symbols represent the same as in Fig. 3.

that the data are fitted at about 85% and 90% confidence level by the exponential and power-law fit, respectively. We are therefore unable to distinguish clearly between an exponential and a power-law radial distribution over the regions observed here with limited sampling and low resolution. A similar conclusion has been pointed out in both Young & Scoville (1982) and Nishiyama et al. (2001). However, Scoville & Young (1983) considered that the exponential distribution was more suitable than that of a power-law for M51. The region in M51 observed by Scoville & Young (1983) is more extended ($\sim 8.5'$) than the region ($\sim 7'$) observed here, and thus the exponential functional form seems to be better for describing the distribution of molecular gas in the whole galaxy. In NGC 3627 and M51, the scale lengths R_0 of the ^{12}CO profiles agree well with the optical K-band scale lengths of 3.5 and 3.2 kpc (Regan et al. 2001), respectively. The results are in line with the finding first noted by Young & Scoville (1982) that the large-scale radial distribution of the ^{12}CO gas follows the light of the stellar disk. In fact, some recent high resolution observations also reveal that the ^{12}CO profiles in a majority of galaxies follow the two-component (bulge and disk) stellar brightness distribution quite well (Regan et al. 2001). The ^{13}CO profiles detected in our

observations are in good agreement with those in Paglione et al. (2001). In NGC 3627 and M51, the ^{13}CO profiles follow similar exponential distributions as ^{12}CO. Because of insufficient data points with significantly high signal-to-noise, however, the detected ^{13}CO data in other galaxies are too limited to reliably present more useful information on their distributions.

Comparing the radial distribution of CO integrated intensities in Figure 3 with the $P - V$ map of CO emission intensities in Figure 4, it is found that the intensities are deficient in the center of NGC 3627, NGC 4631 and M51. However, the centrally deficient feature in molecular ring emission is apparent in NGC 3627 and NGC 4631, but not in M51. So combining the variations in line width shown in Figure 5, we believe the decrement of CO intensity in the central region of M51 is likely to be a result of the dilution in velocity with much wider line width in the center than that in the outer regions of the central disk. On the contrary, the molecular ring emission features with little variations in line width within the bar region in NGC 3627 and NGC 4631 are probably either due to orbital disruption at the inner Lindblad resonance or the central holes with gas exhausted by star formation in the nuclei. Sakamoto et al. (1999) modeled the $P - V$ diagrams to analyze gas distributions and found that the central gas hole is easier to find from $P - V$ diagrams than from integrated intensity maps due to the velocity information.

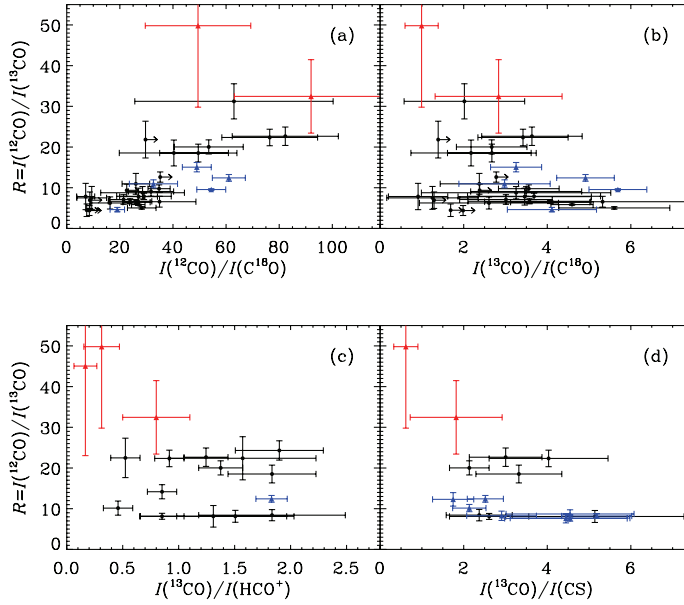## 4.2 Variations in the Intensity Ratio of ^{12}CO to ^{13}CO

Previous studies on the variations of $\mathcal{R}$ in external galaxies have pointed out that some mergers, (U)LIRGs and the central regions of circumnuclear starburst galaxies tend to have higher values of $\mathcal{R}$ than that in normal spiral galaxies (Aalto et al. 1991, 1995; Casoli et al. 1992; Greve et al. 2009; Sage & Isbell 1991), which is similar to that in giant molecular clouds of our Galaxy. Besides the enhancement of ^{12}C caused by nucleosynthesis from type-II SN of massive stars, the deficiency of ^{13}CO caused by isotope-selective photodissociation and the different distributions of ^{12}CO and ^{13}CO were disputed to be alternative reasons for the high $\mathcal{R}$ value for a long time (Aalto et al. 1995; Casoli et al. 1992; Sage et al. 1991; Taniguchi et al. 1999). However, the single-component model calculation of non-LTE CO excitation in Paglione et al. (2001) suggested that the variations of kinetic temperature, cloud column and volume density, as well as starburst superwinds might all contribute to the explanations for the variation in $\mathcal{R}$. Here, we explore the possible causes of the observed variations in $\mathcal{R}$.

4.2.1 Possible causes of variations in $\mathcal{R}$

Our results show that $\mathcal{R}$ varies not only in the nuclei of various types of galaxies, but also within galaxies between nuclear regions and outer disks. The Galactic ^{12}C/^{13}C abundance ratio was found to range from ∼30 at 5 kpc in the Galactic center to ∼70 at 12 kpc (Langer & Penzias 1990). However, this isotopic gradient is opposite to the gradient in the molecular abundance ratio $\mathcal{R}$ (Fig. 3). Therefore, the enhancement of ^{12}C in starburst regions is unlikely to be a correct explanation for the high measured $\mathcal{R}$.

Some authors argue that the selective dissociation of ^{13}CO caused by ultraviolet (UV) fields in massive star formation regions can increase the ratio of $\mathcal{R}$, since the rarer isotope is less shielded from photodissociation (van Dishoeck & Black 1988). Consequently, C^{18}O should be even more dissociated by UV photons than ^{13}CO due to its lower abundance and a positive correlation between $\mathcal{R}$ and the ^{13}CO/C^{18}O intensity ratio would be expected to exist if this is available. However, Figure 6b shows a very marginal anti-correlation between $\mathcal{R}$ and ^{13}CO/C^{18}O with a correlation coefficient $R = -0.34$. Contrary to the expectation, our results reveal a weak anti-correlation, and therefore the deficiency of ^{13}CO caused by isotope-selective photodissociation can be ruled out.

In addition to the high $\mathcal{R}$ measured in M82, the integrated J=2–1/J=1–0 line ratio was found to range between 1.0 and 1.4 (Mao et al. 2000), revealing the existence of highly excited molecular

Fig. 6 Relationship for the normal spiral and starburst galaxies between the integrated intensity ratio of ^{12}CO/^{13}CO. (a) ^{12}CO/C^{18}O, (b) ^{13}CO/C^{18}O, (c) ^{13}CO/HCO$^+$, and (d) ^{13}CO/CS. The black symbols represent the emission of ^{12}CO, ^{13}CO, and C^{18}O in M82 and M51 (in addition to some new detections in IC 342 and NGC 6949) and HCO$^+$ and CS in M82, NGC 3628 and M51. Lower limits (2σ) of the ratio values are denoted with right-pointing arrows for some non-detection of C^{18}O emission. The triangle symbol represents the data taken from literature (see Table 4), the red triangles: NGC 3256, NGC 6240 and Arp 220; the blue triangles: NGC 253, NGC 1808, NGC 2146, NGC 4826 and Circinus. Note that all the ratios have been corrected according to the different beam sizes.

gas. In the PDR model of Mao et al. (2000), it was suggested that the bulk of ^{12}CO emission arises from a warm diffuse interclumpy medium whereas ^{13}CO emission originates in denser cores. In the warm PDRs, the optical depth of ^{12}CO emission from the envelope gas could decrease to a moderate value of $\tau \sim 1$, resulting in the corresponding $\tau(^{13}$CO$) \ll 1$. Moreover, the large concentrations of molecular gas in the nuclear starburst with high T_K can be excited by strong UV emission from young massive stars, shocks and turbulence caused by supernova remnants, and cosmic rays (Pineda et al. 2008; Zhang et al. 2010). The most recent $Herschel$ observations of M82 also suggested that turbulence from stellar winds and supernovae may dominate the heating of warm molecular gas in the central region (Panuzzo et al. 2010). Therefore, it is implied that nonthermal motions produced by the stellar superwinds can broaden ^{12}CO lines, thus enhancing ^{12}CO emission as more photons located deeper in the clouds are allowed to escape. Furthermore, the significantly-high value of $\mathcal{R}$ observed in the spiral arms of M51 also demonstrates that ^{12}CO emission can be enhanced in active star-forming regions compared with that in inter-arm regions.

4.2.2 X-factor and dense gas ratio in extreme starburst

Both theoretical and observational investigations have revealed that ^{12}CO emission is influenced by the intrinsic properties of a molecular cloud (e.g., Pineda et al. 2008; Goodman et al. 2009; Shetty

Table 4 Line Intensity Ratios

Source	$\Delta\alpha$ (′)	$\Delta\delta$ (′)	$I_{^{12}CO}/I_{C^{18}O}$	$I_{^{13}CO}/I_{C^{18}O}$	$I_{^{13}CO}/I_{HCO+}$	$I_{^{13}CO}/I_{CS}$	Reference
M82	0.0	0.0	53.5±13.0	2.7±0.9	1.4±0.2	2.1±0.5	This work
	0.0	0.5	>35.3	>2.8	0.9±0.1	...	This work
	0.0	−0.5	40.5±20.6	2.2±1.4	0.5±0.1	...	This work
	0.5	0.0	82.3±19.5	3.7±1.2	1.2±0.2	3.0±0.9	This work
	0.5	0.5	76.5±18.0	3.4±1.1	0.9±0.1	4.0±1.4	This work
	0.5	−0.5	>29.8	>1.4	1.6±0.7	...	This work
	1.0	0.0	49.5±14.5	2.7±1.1	1.8±0.4	3.3±1.0	This work
	1.0	0.5	63.2±37.5	2.0±1.4	1.9±0.4	...	This work
NGC 3628	0.0	0.0	...	...	0.5±0.1	...	This work
NGC 4631	0.0	0.0	>22.8	>2.4	. . .	. . .	This work
M51	0.0	0.0	29.1±10.3	3.7±1.6	0.9±0.2	2.6±0.9	This work
	0.0	0.5	28.6±15.8	3.3±2.3	1.8±0.7	2.4±0.8	This work
	0.0	1.0	34.9±13.7	5.3±2.8	1.3±0.7	...	This work
	0.0	1.5	9.4±5.6	1.3±1.1	...	...	This work
	0.0	2.0	>7.6	>1.7	...	...	This work
	0.0	2.5	7.1±3.4	0.9±0.7	. . .	. . .	This work
	0.0	−0.5	26.0±5.2	2.4±0.9	1.5±0.5	5.1±2.1	This work
	0.0	−1.0	27.0±7.1	3.5±1.6	...	...	This work
	0.0	−1.5	>8.7	>1.3	. . .	. . .	This work
	0.0	−2.0	>8.6	>2.0	. . .	. . .	This work
M51 disk	. . .	. . .	16.4±7.4	2.6±1.7	. . .	. . .	This work
NGC 253	0.0	0.0	61.0±6.2	4.9±0.7	1.8±0.1	2.5±0.4	[1, 2, 3]
NGC 891	0.0	0.0	...	...	...	4.5±1.4	[3, 4]
NGC 1068	0.0	0.0	...	...	...	1.7±0.5	[3, 5]
NGC 1808	0.0	0.0	48.9±5.4	3.3±0.6	...	...	[6, 7]
NGC 2146	0.0	0.0	32.7±9.1	3.0±1.1	...	...	[6, 7]
NGC 2903	0.0	0.0	...	...	...	4.5±1.5	[3, 4]
NGC 3256	0.0	0.0	91.6±28.1	2.9±1.5	0.8±0.3	1.8±1.1	[8]
NGC 4736	0.0	0.0	...	...	...	4.5±1.5	[3, 4]
NGC 4826	0.0	0.0	19.0±2.7	4.1±1.1	...	...	[6, 7]
NGC 5457	0.0	0.0	...	...	...	2.9±0.8	[3, 4]
NGC 6240	0.0	0.0	...	...	0.2±0.1	...	[9]
Maffei2	0.0	0.0	...	...	...	5.2±0.8	[3, 4]
IC 342	0.0	0.0	35.1±3.0	3.9±0.3	...	2.1±0.4	[1, 3, 4]
Circinus	0.0	0.0	54.4±5.4	5.7±0.7	...	...	[6, 7]
Arp 220	0.0	0.0	49.4±19.9	1.0±0.4	0.3±0.1	0.6±0.3	[9]

All the ratios of integrated intensity have been corrected according to the different beam sizes. [1] Sage et al. (1991); [2] Henkel et al. (1993); [3] Sage et al. (1990); [4] Sage & Isbell (1991); [5] Young & Sanders (1986); [6] Aalto et al. (1991); [7] Aalto et al. (1995); [8] Casoli et al. (1992); [9] Greve et al. (2009).

et al. 2011). In the magneto-hydrodynamic models of Shetty et al. (2011), ^{12}CO integrated intensity is found not to be an accurate measure of the amount of molecular gas, even for ^{13}CO, which may also not be an ideal tracer in some regions. In this case, the much lower opacity C^{18}O can give much more reliable constraints on H_2 column density than optically thick ^{12}CO isotopes. Comparing the H_2 column density derived from ^{12}CO with that from C^{18}O listed in Tables 2 and 3, we find that the amount of molecular gas estimated by the standard Galactic X-factor is consistent with that derived from C^{18}O in M51, whereas it is overestimated in M82 by a factor of 2.5, equal to the ratio of $\mathcal{R}$ between M82 and M51. Consequently, our results confirm that the X-factor adopted in starburst active regions should be lower than that in normal star-forming regions and the gradient in $\mathcal{R}$ can

trace the variations in X-factor. However, surveys of C^{18}O in a larger sample are required to further confirm the relation between the variations in $\mathcal{R}$ and X-factor found in this study.

The average ratio of ^{13}CO to C^{18}O ($\sim 2.9 \pm 1.4$) derived from our observations in M51 and M82 indicates that a portion of ^{13}CO emission has a moderate optical depth, since the ratio of ^{13}CO to C^{18}O should be ~ 7 if both ^{13}CO and C^{18}O lines are optically thin (Penzias 1981). This result is in line with the two-type cloud model suggested in Aalto et al. (1995), in which a large fraction of ^{13}CO emission might originate from a denser gas component. Some previous surveys of dense molecules have provided support for the presence of such dense gas (e.g., Sage et al. 1990; Nguyen et al. 1992; Gao & Solomon 2004a). Our detection of HCO$^+$ and CS in M82 and M51 is consistent with that in both Sage et al. (1990) and Naylor et al. (2010). The ratios of ^{13}CO to HCO$^+$ and ^{13}CO to CS in (U)LIRGs NGC 3256, NGC 6240 and Arp 220 (Casoli et al. 1992; Greve et al. 2009) are found to be lower than those in the nuclear regions of normal spirals and M82 (Fig. 6), which probably indicate that the dense gas fraction is higher for these (U)LIRGs, since ^{13}CO can be considered as a relatively reliable tracer of total molecular gas due to its low abundance. This result agrees well with the conclusion in Gao & Solomon (2004b) that galaxies with high star formation efficiency (SFE) tend to have higher dense gas fraction. Moreover, the ratio $\mathcal{R}$ values measured in NGC 3256, NGC 6240 and Arp 220 are found to be much higher than those in M82 (Fig. 6), which is likely to imply that the bulk of ^{12}CO emission arising from warm diffuse gas is enhanced in conditions of extreme starburst.

Summarizing the above analysis, the systematical gradient in $\mathcal{R}$ can be explained by the variations in the physical conditions of molecular gas. The standard Galactic X-factor used in M82 overestimates the amount of molecular gas by a factor of 2.5, and the variations in X-factor can be well traced by the gradient in $\mathcal{R}$. Nevertheless, additional observations of both ^{12}CO and ^{13}CO lines at $J \geq 2$ and C^{18}O emission are required to better constrain the physical conditions of the molecular gas in external galaxies.

5 SUMMARY

We simultaneously observed the ^{12}CO, ^{13}CO and C^{18}O emission lines in 11 nearby brightest infrared galaxies, of which four (NGC 3627, NGC 3628, NGC 4631 and M51) were mapped with half-beam spacing along the major axes and M82 was fully mapped in an area of $4' \times 2.5'$. These are the first systematic extragalactic observations for the PMO 14 m telescope and the main results are summarized as following:

(1) We detected the ^{12}CO emission towards 99 of the positions observed, with the ^{13}CO seen towards 51 of these. C^{18}O was detected at 13 positions close to the nuclear regions in M51 and M82, among which the off-center positions in M51 reported here were the first C^{18}O detection.
(2) In the four galaxies with major axes being mapped, the ^{13}CO line intensity decreases from the center to the outer disk, similar to that of ^{12}CO. In NGC 3627, NGC 3628 and M51, the radial distribution of both ^{12}CO and ^{13}CO can be well fitted by an exponential function, whereas the ^{12}CO distribution in NGC 4631 is better fitted by a power-law. The scale length of ^{12}CO emission is about $0.2\,R_{25}$ with a mean value of ~ 3 kpc. Moreover, the ^{12}CO scale lengths in NGC 3627 and M51 are in good agreement with the optical scale lengths.
(3) The peak velocity of ^{12}CO rotation curves ranges from 120 to 240 km s^{-1}, and the line widths of ^{12}CO lines tend to drop with radius from center to outer disk in all mapped galaxies. Of all positions observed, the distribution of both line intensity and profiles of ^{12}CO and ^{13}CO have good agreement, as expected with simultaneous ^{12}CO and ^{13}CO observations.
(4) A decreasing tendency of $\mathcal{R}$ with radius from center to outer disk is found in mapped galaxies. $\mathcal{R}$ varies from 3.3 ± 0.7 to 24.8 ± 2.5 in positions with both ^{12}CO and ^{13}CO detected. The average $\mathcal{R}$ values are 9.9 ± 3.0 and 5.6 ± 1.9 in the center and disk regions of normal spiral galaxies, respectively.

(5) The high $\mathcal{R}$ measured in M82 is likely to be caused by enhanced ^{12}CO emission from deeper cloud regions with the broad ^{12}CO line produced by the stellar winds and supernovae. The low values of ^{13}CO/C^{18}O ($\sim$2.8$\pm$1.2) found in M82 support the suggestion that a considerable fraction of ^{13}CO emission originates in a denser gas component. Comparing the ratios of ^{13}CO/HCO^{+} and ^{13}CO/CS in normal galaxies with those in U/LIRGs, the lower values found in U/LIRGs agree with the notion that the galaxies with high SFEs tend to have a higher dense gas fraction.

(6) Comparing with the H$_2$ column density derived from C^{18}O, the standard Galactic X-factor is found to overestimate the amount of molecular gas in M82 by a factor of $\sim$2.5. This confirms the assertion that a lower X-factor should be adopted in active starburst regions than that in normal star-forming disks, and moreover, the gradient in $\mathcal{R}$ can be used to reliably trace the variations of the X-factor.

Appendix A: THE STABILITY OF THE DELINGHA RADIO TELESCOPE

Figure A.1 is an Allan Variance Plot, which is often the ultimate way to measure stability but requires an enormous amount of observation time. There are three main contributions to be aware of in the Allan plot, including the white noise, the $1/f$-noise and low frequency drift noise.

The upper panel of Figure A.1(a) shows how the squared RMS noise of ^{12}CO spectra with velocity resolution of $\sim$0.16 km s^{-1} varied with the integration time on source, while the lower panel shows the relative error deviations from the radiometer equation. The radiometer equation, as
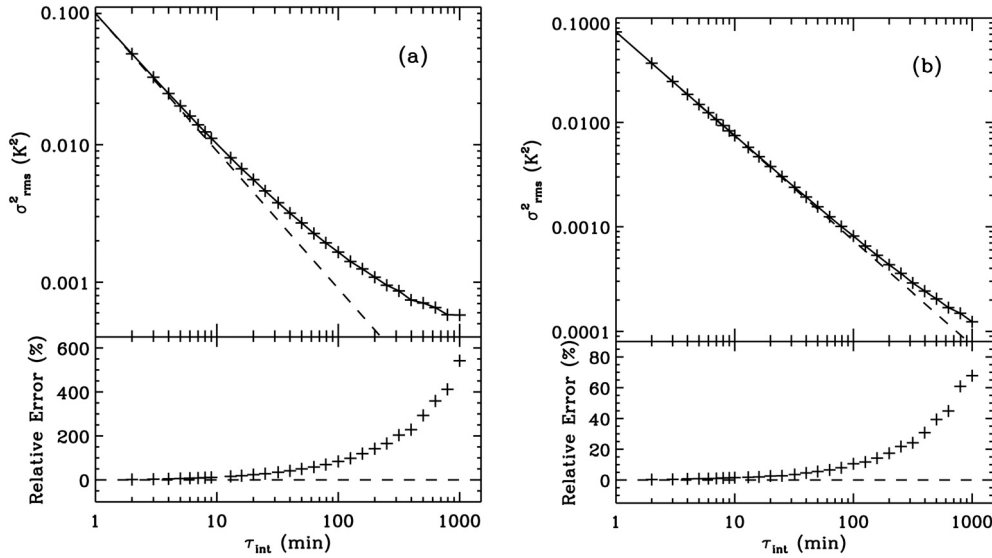
Fig. A.1 Allan Variance and the relative error from the radiometer equation as a function of integration time on the source (see Appendix A). In the upper panel of each figure, the dashed line represents what is expected from the radiometer equation with a slope of -1. In the lower panel, each point represents the relative error between the value that is measured and expected from the radiometer equation. (a) The data taken from the observing semester of 2008 to 2009. (b) The data taken from the observing semester of 2009 to 2010.

well as the limiting sensitivity of the spectrometer, is given by

$$\frac{\Delta T_{\mathrm{rms}}}{T_{\mathrm{sys}}} = \frac{K}{\sqrt{\Delta \nu \tau}} \,, \tag{A1}$$

where T_{sys} is system temperature, τ is the sum of the integration time on the source and in the off position, K is a factor accounting for data acquisition procedures, and ΔT_{rms} is rms noise temperature of the spectra for a given frequency resolution $\Delta \nu$.

Figure A.1(a) and (b) show the data obtained from the observing semesters of 2008 to 2009 and of 2009 to 2010, respectively. It can be seen in Figure A.1(a) that the Allan plot begins to deviate from the radiometer equation when integrating about 10 minutes on the source, and the relative error increases to 80% when integrating 100 minutes, however, it is shown in Figure A.1(b) that the relative error increases to only 10% with the same integration time. Therefore, both the stability and the sensitivity of the telescope have been greatly improved after the system maintenance in the summer of 2009. The average noise level on the temperature scale of T_A^* would be 0.020 K and 0.018 K when integrating 100 and 200 minutes on source respectively, with a spectral velocity resolution of $\sim$10 km s^{-1}. Therefore, this plot can be used to estimate observation time according to the sensitivity that we required. However, an important thing to note in this Allan Variance Plot is that the data we used are the raw data, that is to say, we did not perform any data processing, such as rejecting the spectra with distorted baseline or abnormal rms noise level. Consequently, we could get even better sensitivity if we just co-added the spectra that were found to be consistent within the normal rms noise level. Based on these analyses, it seems that the telescope still has the capability to detect an even weaker emission signal than what has been detected, since the effective integration time of most of our observations has not reached the limit.

References

Aalto, S., Booth, R. S., Black, J. H., & Johansson, L. E. B. 1995, A&A, 300, 369
Aalto, S., Black, J. H., Johansson, L. E. B., & Booth, R. S. 1991, A&A, 249, 323
Allen, R. J., & Lequeux, J. 1993, ApJ, 410, L15
Bohlin, R. C., Savage, B. D., & Drake, J. F. 1978, ApJ, 224, 132
Bolatto, A. D., Leroy, A. K., Rosolowsky, E., Walter, F., & Blitz, L. 2008, ApJ, 686, 948
Braine, J., Combes, F., Casoli, F., et al. 1993, A&AS, 97, 887
Casoli, F., Dupraz, C., & Combes, F. 1992, A&A, 264, 49
Daddi, E., Elbaz, D., Walter, F., et al. 2010, ApJ, 714, L118
Dahmen, G., Huttemeister, S., Wilson, T. L., & Mauersberger, R. 1998, A&A, 331, 959
Dame, T. M., Hartmann, D., & Thaddeus, P. 2001, ApJ, 547, 792
Dickman, R. L. 1978, ApJS, 37, 407
Downes, D., & Solomon, P. M. 1998, ApJ, 507, 615
Evans, N. J., II 1999, ARA&A, 37, 311
Frerking, M. A., Langer, W. D., & Wilson, R. W. 1982, ApJ, 262, 590
Gao, Y. 1996, Dense Molecular Gas in Galaxies and the Evolution of Luminous Infrared Galaxies, Ph.D. Thesis, State University of New York at Stony Brook
Gao, Y., & Solomon, P. M. 2004a, ApJS, 152, 63
Gao, Y., & Solomon, P. M. 2004b, ApJ, 606, 271
Goodman, A. A., Pineda, J. E., & Schnee, S. L. 2009, ApJ, 692, 91

Greve, T. R., Papadopoulos, P. P., Gao, Y., & Radford, S. J. E. 2009, ApJ, 692, 1432

Helfer, T. T., Thornley, M. D., Regan, M. W., et al. 2003, ApJS, 145, 259

Henkel, C., Mauersberger, R., Wiklind, T., et al. 1993, A&A, 268, L17

Hunter, S. D., Bertsch, D. L., Catelli, J. R., et al. 1997, ApJ, 481, 205

Israel, F. P. 1997, A&A, 328, 471

Langer, W. D., & Penzias, A. A. 1990, ApJ, 357, 477

Leroy, A. K., Walter, F., Bigiel, F., et al. 2009, AJ, 137, 4670

Maloney, P., & Black, J. H. 1988, ApJ, 325, 389

Mao, R. Q., Henkel, C., Schulz, A., et al. 2000, A&A, 358, 433

Matthews, L. D., & Gao, Y. 2001, ApJ, 549, L191

Naylor, B. J., Bradford, C. M., Aguirre, J. E., et al. 2010, ApJ, 722, 668

Nguyen, Q., Jackson, J. M., Henkel, C., Truong, B., & Mauersberger, R. 1992, ApJ, 399, 521

Nishiyama, K., Nakai, N., & Kuno, N. 2001, PASJ, 53, 757

Paglione, T. A. D., Wall, W. F., Young, J. S., et al. 2001, ApJS, 135, 183

Panuzzo, P., Rangwala, N., Rykala, A., et al. 2010, A&A, 518, L37

Penzias, A. A. 1981, ApJ, 249, 518

Pineda, J. E., Caselli, P., & Goodman, A. A. 2008, ApJ, 679, 481

Regan, M. W., Sheth, K., & Vogel, S. N. 1999, ApJ, 526, 97

Regan, M. W., Thornley, M. D., Helfer, T. T., et al. 2001, ApJ, 561, 218

Rickard, L. J., & Blitz, L. 1985, ApJ, 292, L57

Sage, L. J., Mauersberger, R., & Henkel, C. 1991, A&A, 249, 31

Sage, L. J., & Isbell, D. W. 1991, A&A, 247, 320

Sage, L. J., Shore, S. N., & Solomon, P. M. 1990, ApJ, 351, 422

Sakamoto, K., Okumura, S. K., Ishizuki, S., & Scoville, N. Z. 1999, ApJS, 124, 403

Sanders, D. B., Mazzarella, J. M., Kim, D., Surace, J. A., & Soifer, B. T. 2003, AJ, 126, 1607

Sanders, D. B., & Mirabel, I. F. 1996, ARA&A, 34, 749

Sato, F., Mizuno, A., Nagahama, T., et al. 1994, ApJ, 435, 279

Scoville, N., & Young, J. S. 1983, ApJ, 265, 148

Scoville, N. Z., & Solomon, P. M. 1974, ApJ, 187, L67

Scoville, N. Z., Yun, M. S., Clemens, D. P., Sanders, D. B., & Waller, W. H. 1987, ApJS, 63, 821

Shetty, R., Glover, S. C., Dullemond, C. P., & Klessen, R. S. 2011, MNRAS, 11

Sodroski, T. J., Odegard, N., Dwek, E., et al. 1995, ApJ, 452, 262

Soifer, B. T., Houck, J. R., & Neugebauer, G. 1987, ARA&A, 25, 187

Solomon, P. M., & Sage, L. J. 1988, ApJ, 334, 613

Solomon, P. M., & Vanden Bout, P. A. 2005, ARA&A, 43, 677

Sparke, L. S., & Gallagher, J. S., III 2000, Galaxies in the Universe: an Introduction, eds. Linda S. Sparke and
        John S. Gallagher, III (Cambridge: Cambridge University Press), 416

Taniguchi, Y., Ohyama, Y., & Sanders, D. B. 1999, ApJ, 522, 214

van Dishoeck, E. F., & Black, J. H. 1988, ApJ, 334, 771

Vila-Vilaró, B. 2008, PASJ, 60, 1231

Wilson, T. L., Rohlfs, K., & Hüttemeister, S. 2009, Tools of Radio Astronomy, eds. Thomas L. Wilson, Kristen
        Rohlfs & Susanne Hüttemeister (Berlin: Springer-Verlag)

Young, J. S., & Sanders, D. B. 1986, ApJ, 302, 680

Young, J. S., & Scoville, N. 1982, ApJ, 258, 467

Young, J. S., & Scoville, N. Z. 1991, ARA&A, 29, 581

Young, J. S., Xie, S., Tacconi, L., et al. 1995, ApJS, 98, 219

Zhang, Z., Gao, Y., & Wang, J. 2010, Science in China G: Physics and Astronomy, 53, 1357